Journal of Alloys and Metallurgical Systems 7 (2024) 100097

Contents lists available at ScienceDirect

Journal of Alloys and Metallurgical Systems

journal homepage: www.journals.elsevier.com/journal-of-alloys-and-metallurgical-systems

Structural analysis of selective laser melted copper-tin alloy

Ramin Rahmani [a,b,*], Pedro R. Resende [b], Rúben Couto [b], Sérgio I. Lopes [a,c], Rahul Kumar [d], Himanshu S. Maurya [e,f], Javad Karimi [g,h], Alexandre M. Afonso [i], Abrar Hussain [e], João C.C. Abrantes [b]

[a] CiTin, Centro de Interface Tecnológico Industrial, Arcos de Valdevez 4970-786, Portugal
[b] proMetheus, Instituto Politécnico de Viana do Castelo (IPVC), Viana do Castelo 4900-347, Portugal
[c] ADiT-Lab, Instituto Politécnico de Viana do Castelo (IPVC), Viana do Castelo 4900-347, Portugal
[d] Laboratory for Tribology and Interface Nanotechnology (TINT), University of Ljubljana, Askerceva 6, Ljubljana SI-1000, Slovenia
[e] Tallinn University of Technology, Department of Mechanical and Industrial Engineering, Ehitajate tee 5, Tallinn 19086, Estonia
[f] Luleå University of Technology, Department of Engineering Sciences and Mathematics, Luleå SE 97187, Sweden
[g] BIAS, Bremer Institut für angewandte Strahltechnik GmbH, Klagenfurter Straβe 5, Bremen 28359, Germany
[h] Institute of Materials Engineering, Technische Universität Bergakademie Freiberg, Gustav-Zeuner-Str.5, Freiberg 09599, Germany
[i] CEFT, Transport Phenomena Research Center, Department of Mechanical Engineering (FEUP), University of Porto, Portugal

ARTICLE INFO

Keywords:
Copper alloys
Thermal conductivity
Electrical conductivity
Selective laser melting
Additive manufacturing

ABSTRACT

Additively manufactured complex geometries from copper alloys with high thermal and mechanical properties have drawn the attention of researchers. The present contribution explores the additive manufacturing (AM) of copper-based alloys from powder particles intended for heat sink and heat exchange applications. Selective laser melting (SLM) parameters featuring low laser beam power (160 W), moderate scanning speed (320 mm/s), and high energy density (200 J/mm^3) were employed to fabricate dense components from CuSn10 particles. The present work deal with structural analysis and precision investigation of microfabrication, particularly in Struts, Tubes, and Fins. Mechanical properties (compression and hardness) for Strut structure, differential pressure evaluations for Tube structure, and analyses of thermal and electrical conductivities for Fin structure were investigated. The results showed an improvement in strength compared to those of pure copper, facilitating ease of AM. The obtained results affirm the feasibility of AM, demonstrating the successful creation of complex and combined solid-porous structures using SLM process from Cu alloys. A comprehensive structural investigation and characterization of the Cu–Sn alloy is presented here, aiming to establish a standardized approach for analysing Cu alloys. The results indicate that small-scaled structures fabricated via CuSn10 alloy exhibits a thermal conductivity of 34.3 W·m^{-1}·K^{-1}, an electrical conductivity of 4.72×10^6 S/m, a hardness of 119 HV-50, a uniform surface roughness of 6 μm, and can withstand a force loading of 1 kN.

1. Introduction

Additive Manufacturing (AM) technologies have revolutionized the production of intricate metal components, offering unprecedented flexibility and rapidity in design and fabrication. Among these, Selective Laser Melting (SLM) has emerged as a cutting-edge process for 3D printing, enabling the creation of complex and high-performance structures [1,2]. The utilization of low-alloyed copper alloys, such as CuSn10, CuCr1Zr, CuNi2SiCr, CuAl10, etc., is driven by the inherent challenges posed by the high thermal conductivity of pure copper [3]. This alloying strategy enhances printability and ensures better melt pool stability, subsequently reducing the risks of cracking and distortion during rapid solidification. The pre-alloyed copper ability to promote better layer adhesion plays a crucial role in minimizing thermal stresses. Additionally, the alloying process facilitates the development of a finer grain structure and offers control over phase transformations during the cooling process [4].

Among Cu alloys, Cu–Sn alloys exhibit improved wear resistance and cost-effective, making them suitable for various applications, such as heatsinks. Tin improves the alloy's mechanical property, then CuSn10 might be more cost-effective compared to Cu15Ni8Sn or gas-atomized pure copper in mass production. It has been reported that the addition

* Corresponding author at: CiTin, Centro de Interface Tecnológico Industrial, Arcos de Valdevez 4970-786, Portugal.
E-mail addresses: ramin.rahmaniahranjani@gmail.com, ramin.rahmani@citin.pt (R. Rahmani).

https://doi.org/10.1016/j.jalmes.2024.100097
Received 4 June 2024; Received in revised form 16 July 2024; Accepted 29 July 2024
Available online 3 August 2024
2949-9178/© 2024 The Authors. Published by Elsevier B.V. This is an open access article under the CC BY license (http://creativecommons.org/licenses/by/4.0/).

of tin to copper alloys can enhance wear resistance, making it suitable for applications where parts are subjected to friction. On the other hand, the presence of nickel enhances strength and corrosion resistance for its related applications [5]. However, nickel price (in Cu–Ni–Sn alloy) is more expensive than copper and tin, so the overall cost of the Cu15Ni8Sn alloy may be higher than CuSn10.

The primary objective has consistently been to optimize the compressive strength, physical-mechanical properties such as surface roughness, density, hardness, and technology readiness level (TRL), and measure the electrical/mechanical conduction for thermal management devices in both porous and solid forms of copper alloys, using the SLM process. It is notable that existing studies, while limited, have primarily focused on optimizing the processing parameters of SLM copper or comparing it to copper alloys. There has been comparatively less exploration of their electrical and thermal properties, which are inherent strengths of copper [6]. An interesting approach in the literature involves investigating low-alloyed copper (comprising 90 % Cu or more) instead of pure Cu to achieve better thermal control and increased laser absorption. Additionally, there is a trend toward exploring lattice structures instead of bulk samples, showcasing the laser powder bed fusion (L-PBF) capability to produce intricate shapes. SLM is a specific type of Laser Powder Bed Fusion (L-PBF, ASTM F2792 standard); L-PBF is a broad category that includes various processes using a laser to fuse metal powders. For instance, Ma et al. [7] observed uniformity in the CuCr1Zr lattice structures without cell breakage or strut fracturing under compression deformations, a goal that is also pursued in the current article for CuSn10.

The utilization of pre-alloyed copper instead of pure in SLM process (by adding low percentage of Sn, Zr, Cr, Al and Si) helps achieve the desired balance of thermal conductivity and mechanical strength in the additively manufactured components. Despite SLMed components of copper have a large potential application due to its outstanding thermal and electrical conductivity, however, it shows challenging printability, high defects density (e.g., crack and porosity), poor mechanical properties, and shaping the complex geometry. This limitation arises from its high thermal conductivity and the tendency to form oxide layers [8,9]. One solution involves the high energy absorptivity of Cu through a SLM device equipped with a green laser (~500 nm) and it facilitates the creation of a stable molten pool [10]. Another option is to employ conventional L-PBF approach, typically utilizing an infrared laser (~1000 nm) with low laser power [11]. This approach aims to enhance the absorption rate, heating and cooling rates, consolidation, and structural precision during the additive manufacturing process. Lower laser power reduces energy consumption, leading to significant cost savings, particularly in large-scale and mass production. This makes the process more economically viable for a wider range of applications and developing low-power and lab-sized SLM systems can make the technology more accessible to small and medium-sized enterprises (SMEs).

With a low laser power, there may be a risk of insufficient energy being delivered to the material, leading to incomplete melting or inadequate layer merging, especially for highly reflective metals like copper and its alloys, particularly in the visible and near-infrared regions of the electromagnetic spectrum. For applying commercial SLM devices that are normally limited to lower power (~500 W) and higher wavelength (~1000 nm), there is a need to optimize the other parameters for successful fabrication of both solid and porous structures [12]. The microstructures and mechanical properties of AMed Cu alloys such as Cu–Ni–Sn and Cu–Cr–Zr have been extensively studied in the literature [13,14], however, complex shapes with varying volume fractions, lattice structures, porous structures, triply periodic minimal surfaces (TPMS) need to be further investigated [15,16]. This is due to the advantages offered by AM compared to subtractive manufacturing (SM). In the context of Cu alloy applications in small-scale devices, it is crucial to standardize tests for load-bearing lattice structures, formulate fluid flow characteristics for hollow cylinders, and determine thin sheet thermo-electrical conductivity.

The present work focuses on the dense SLMed CuSn10 copper components, tailored for heat sink and heat exchange applications. The exploration of this advanced manufacturing technique involves a meticulous examination of structural architectures such as Struts (linear rods), Tubes (hollow cylindrical), and Fins (rectangular surfaces), with an emphasis on microfabrication precision. By employing a commercial SLM device with low laser power and a tailored infrared wavelength spectrum, this study delves into the structural discussion of small-scaled thin, cylindrical and flat shapes. Besides the density, roughness and micrograph analyses, the investigation spans compression tests for load-bearing Strut structures, pressure evaluations for Tube structures, and analyses of thermal and electrical conductivities for Fin structures, collectively affirming the feasibility of rapid prototyping for intricate copper-based structures.

2. Materials and methods

Gas-atomized CuSn10 powder particles, balanced with copper and featuring a particle size range of 20–63 μm with 10 % Tin content, is provided by ECKART TLS GmbH, Germany. The fabrication of structures in this study utilizes the TruPrint 1000 device from Trumpf GmbH, Germany, known for its compactness and rapid productivity in SLM process. The TruPrint 1000 system boasts a maximum power of 500 W, a cylindrical built volume of Ø 97 x H 100, and a laser beam diameter of 200 μm. The layer thickness for various components, including support, solid parts, and main structures, is standardized at 25 μm. Consistent parameters such as applied power and scanning speed are maintained at 160 W and 320 mm/s, respectively, across all samples.

Energy density (E, J/mm^3) has direct proportional to the laser power (P, W) and inverse proportional to scanning speed (v, mm/s), hatch spacing (mm), and layer thickness (t, mm) [17], which is determined by Eq. 1.

$$E = \frac{P}{v.h.t} = \frac{160 \quad W}{320\,\frac{mm}{s} \times 0.1mm \times 0.025mm} = 200 \quad \frac{J}{mm^3} \tag{1}$$

For low laser power, reducing the scanning speed is crucial to avoid the balling phenomenon (sticked/unmelted powders) during the melting process. Based on this equation, instead of increasing the laser power, we considered reducing the scanning speed and layer thickness to achieve densification [18]. Increasing the energy density improves wetting ability of metal and achieves better densification with lower porosity. However, due to copper's thermal conductivity and the risk of distortion or evaporation, energy density cannot be increased beyond a certain limit.

The CuSn10 powder's scanning electron microscope (SEM) micrograph is presented in Fig. 1. The average flow rate of CuSn10 powder is 16 s/50 g, with a density of $\geq$ 4.7 g/cm^3. Particle size analysis and measurements were conducted using the Mastersizer 3000 Hydro, manufactured by Malvern Instrument Ltd. (United Kingdom), which has a range of 0.01–3500 μm. The particle size by density and distribution for the CuSn10 powder is depicted in Fig. 2.

An average flow rate of 16 s/50 g indicates that 50 g of powder flows through a specified orifice in 16 seconds under standardized conditions. Powders with a flow rate under 30 s/50 g are typically considered to have good flowability for SLM [19]. However, satellite particles and agglomeration can form large clusters, reducing flowability and creating gaps in the powder bed [20]. To address this, we reduced the layer thickness to 25 μm, increasing energy density and consolidation, and preheated the powder at 150°C for 3 hours before using it in the SLM device.

The Hitachi SU1510 VP-SEM from Japan integrates a high-performance and compact SEM with a beam energy range of 300 eV to 30 keV, delivering a single exposure resolution of 3 nm in high-vacuum mode (15 kV). This SEM is utilized for micrography of samples and assessing the surface roughness of structures. For X-ray

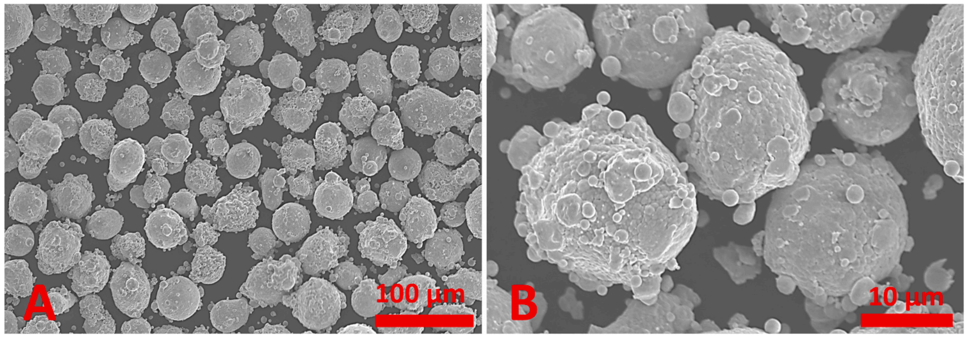

Fig. 1. SEM micrograph of CuSn10 powder with A) low and B) high magnification.

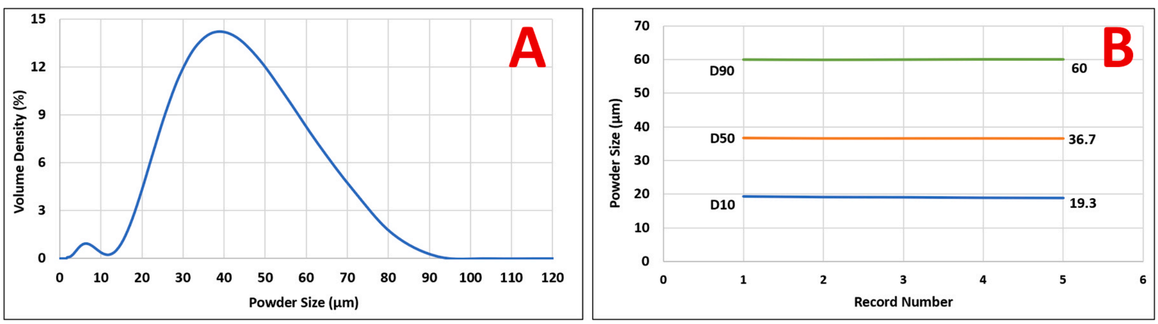

Fig. 2. Analysis of for CuSn10 powder; A) Volume density plot, B) Particle size distribution.

diffraction (XRD), the D8 Advance by Bruker (Germany) is employed to investigate scattering, phase identification, phase analysis, structure analysis, and texture. It has copper (Cu–Kα) source and step size of 0.02° (2θ) and 1 s step time was selected for the measurements. The compression test on the Strut structure is conducted using the Shimadzu AG-X plus (100 kN, Japan), known for its short-column type design, allowing precise control over force-displacement-time parameters for assessing lattice or strut fracturing. Thermal conductivity measurement of a cylindrical solid CuSn10 sample (diameter Ø20 mm, height 20 mm) is performed using the Armfield HT11C linear heat conduction method. In this technique, a heat source is applied to one side of the material, while a temperature sensor on the opposite side measures the temperature change across the material over time, following Fourier's law of heat conduction. Additionally, this Ø20 × H20 mm CuSn10 sample will be utilized for density measurements using the Archimedes immersion method.

The hardness testers from the DuraVision G5-Series, manufactured by Emco-Test GMBH in Austria, encompass an exceptionally broad standard load range spanning from 0.3 to 250 kgf. This precision instrument enables the measurement of Rockwell, Brinell, and Vickers test methods in accordance with EN ISO and ASTM standards. It is notable that various hardness tests were conducted five times on both the top and bottom sides of a vertically 3D-printed solid cylinder sample with dimensions Ø20 × H20 mm. The sample was lightly polished using P400/P800 grit sandpapers (without heat treatment). For the measurement of fluid flow through the tube, including assessments of flow stability and inner roughness, the differential pressure was measured using SM5852 Series piezoresistive differential pressure transducers, while the flow rate was measured using Nemesys low pressure syringe pump equipment.

With a research focus on structural analysis and manufacturing precision, three distinct structures are designed: Struts (linear rods with a diameter of Ø 200 µm), Tubes (hollow cylindrical pipes with an inner diameter of Ø 0.5 mm and outer diameter of Ø 1 mm), and Fins

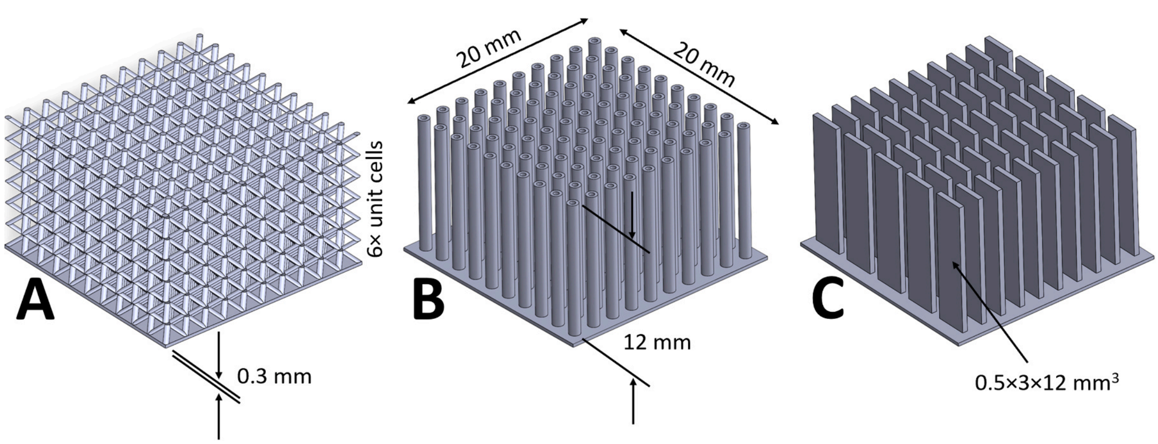

Fig. 3. CAD model of A) *Strut* structure; 6 cells with unit size of 2×2×2 mm, B) *Tube* structure; 10×10 hollow cylinders with inner diameter of Ø 0.5 and outer Ø 1 mm, C) *Fin* structure; 5×10 blocks with size of 0.5×3×12 mm. All samples have 0.3 mm solid base, 12 mm height and 20×20 mm base area.

(rectangular cubes with dimensions of 0.5×3×12 mm). As illustrated in Fig. 3, these architectures are created to manufacture and evaluate the capability of low-alloyed copper through the SLM process for supporting complex-shaped, micro-piping, and small-scale heatsink applications. The computer-aided design (CAD) of samples is accomplished using *SolidWorks* software, while the preparation for the 3D printer is managed with *Materialise Magics* software.

3. Results and discussion

The AMed copper-tin alloy (Cu–Sn) is of high interest for various applications. Because of its excellent thermal and electrical conductivity, the 3D complex heat exchangers and customized electronic components can be fabricated. Bearings and bushings can be fabricated from Cu–Sn due to its sufficient printability, good mechanical properties and biocompatibility, and effectiveness against bacteria [21,22]. Porosity represents a significant challenge during sintering; In addition to optimizing SLM parameters, the addition of hard materials can greatly enhance wear resistance [23,24]. Laser power, laser wavelength, scanning speed, powder dimensions, layer thickness, thermal management, support design and topology of structure are main parameters need to be matched together for a successful L-PBF manufacturing of the copper alloy architecture, which the terminology is standardized based on ASTM F2792 for additive manufacturing. In the context of SLM, scanning speeds can range from relatively low values (e.g., below 100 mm/s) to high values (e.g., above 1000 mm/s). The designed strategy used in the present article is lower laser power and higher scanning speed for support part (100 W and 700 mm/s), versus higher laser power and lower scanning speed for the main structure (160 W and 320 mm/s).

Fig. 4 shows the XRD pattern of the CuSn10 particles and the AMed part via SLM process. The XRD of the particles indicates a mixture of α-Cu and intermetallic compound phase (δ-Cu40.5Sn11), which is similar to those reported by [25,26]. The SLMed samples also illustrated a mixture of both phases, i.e., Cu- (α-Cu) and Sn-rich (intermetallic) phases. Zeng et al. [27] studied XRD of the SLMed samples in longitudinal and transverse direction, and concluded a shift of α phase peak because of Sn diffusion into α phase during AM.

3.1. Strut structure

The structures designed in Fig. 3 are fabricated on a 100 mm platform of copper using the SLM device, as configuration is depicted in Fig. 5. Parameters such as unit cell, pore size, and strut diameter of the lattice are crucial in defining the weight and volume fraction of the lattice (Strut) structure. These parameters directly impact the load-bearing capacity and other mechanical properties of the structure. SEM micrographs of the Strut structure at various views and magnifications are presented in Fig. 6, corresponding to a 200 µm beam diameter, approximately 33 % volume fraction, and a 2×2×2 mm^3 unit cell. During the consolidation or recoater sweeping in the SLM process, unmelted powder particles adhering to the outer diameter of the beams significantly influence the strength, accuracy, and weight of the structure, especially for small strut diameters [28,29].

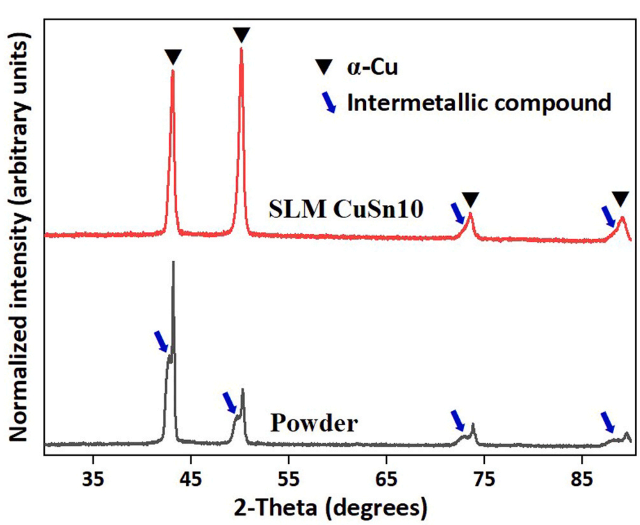

Fig. 4. X-Ray diffraction analysis of CuSn10 powder and SLMed parts.

The cutting and post-processing of copper parts pose greater challenges compared to some other metals. The support structure assumes a crucial role, as the absence of a solid bottom part hinders the effective connection between the platform and the main structure. Conversely, a porous design is required in the support structure to facilitate easy cutting and prevent shielding stress and thermal distortion. The final samples feature a 0.3 mm solid bottom (comprising 12 layers with a thickness of 0.025 mm each), a 3 mm designed porous support for cutting, followed by another 0.3 mm solid part on top to establish a connection with the main sample. The support design, along with its scanning electron microscopy (SEM) micrograph, is illustrated in Fig. 7.

The compression test of the Strut structure (lattice) from Cu–Sn with 12 mm height is shown in the graph in Fig. 8, where the relationship between force (N) and displacement (mm) can be observed. during a compression test on a Strut (lattice) structure with 12 mm height. In the initial phase, up until around 7 mm of displacement, there is a moderate increase in force. This indicates that the lattice structure was relatively stable and could withstand compressive forces. However, beyond approximately 7 mm of displacement, there is an abrupt increase in force. This could imply that at this point, the lattice structure starts undergoing significant deformation or failure. This sharp rise suggests that the structure has reached its limit of elasticity and has begun to deform plastically. Prior to reaching the yielding point under the applied load, the Strut structure exhibits resistance, with an approximate displacement of 9 mm under a force of 1000 N. During this test, there were no instances of cell breakage or strut fracturing observed subjected to compression deformations.

3.2. Tube structure

The primary objective in creating Tube structure is to develop diverse designs of thermal management devices (TMDs) to enhance microchannel cooling systems in the electronic industry [30]. Pure and low-alloyed copper emerges as an outstanding material for heat exchangers, thanks to its exceptional attributes such as high thermal conductivity, fatigue strength, creep rupture strength, resistance to corrosion, resistance to biofouling, maximum allowable stress and internal pressure, specific heat, thermal expansion, antimicrobial properties, tensile and yield strength, and ease of formation and joining.

To understand the flow dynamics inside of a 3D printed heat exchange system, a fluid test was performed in a copper tube fabricated using SLM. The main objective is to verify flow stability regarding the dimensional precision of the tube, specially to understand the internal frictional resistance caused by the unmelted powder particles sticked to surface of the tube structure. The tube has an inner diameter (d) of ~0.5 ± 0.0088 mm and a length (L) of ~12 mm, as shown in Fig. 9, where an SEM micrograph of the tube structure is presented. Flow stability, dimensional precision, internal friction, and the presence of unmelted particles are four crucial for determining a consistent flow rate. The tube has an inner diameter of 0.5 mm and a thin wall of 0.25 mm, making measurement challenging, especially as the length increases or the diameter decreases.

1. Flow stability is smoothness of the fluid flow through the tube. Inconsistent flow can lead to turbulence, which increases energy losses and reduces the efficiency of the system. For applications requiring precise thermal management or fluid transport, stable flow

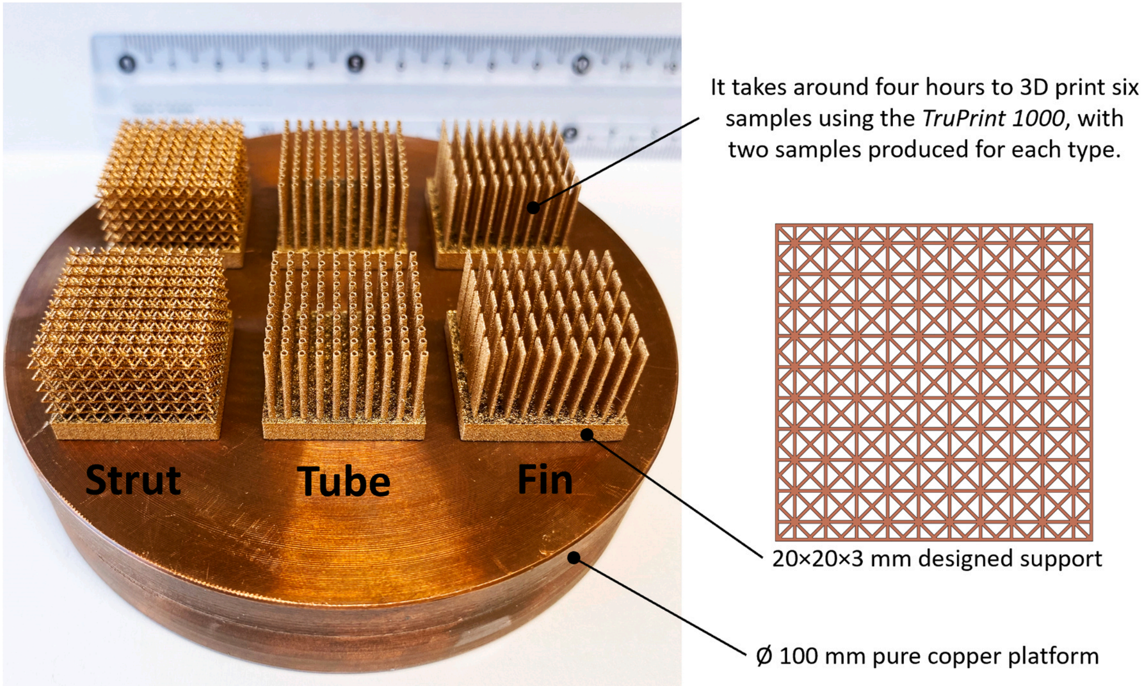

Fig. 5. SLMed three types of structures. A 3 mm height designed support is strategically positioned between the platform and samples. This support is intended for easy post-printing cutting, prevention of distortion caused by the thermal conductivity of structures and ensuring sufficient strength to withstand rubber wiping without separation.

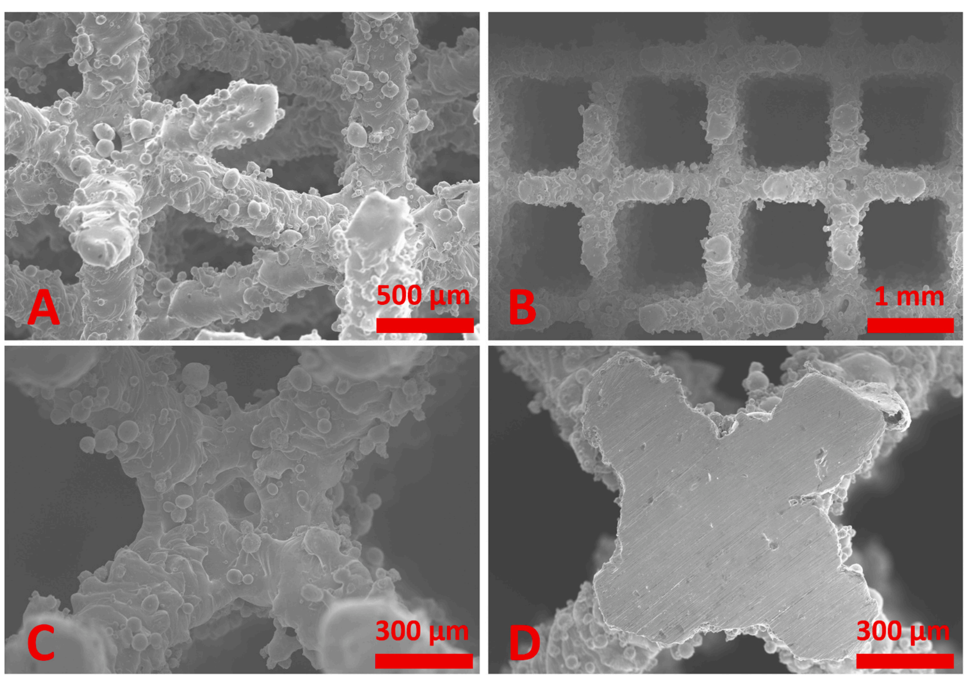

Fig. 6. SEM micrograph of as-built Strut structure, fabricated using SLM process: A, B and C) Struts and cells and accuracy in different magnifications, D) Refined area of last layer for considering of densification.

ensures predictable performance and optimal heat transfer, and avoiding of pressure fluctuations and mechanical stresses.

2. Precise dimensions ensure that the flow path is uniform, minimizing areas where fluid velocity can vary significantly. In SLM process, achieving high dimensional accuracy can be challenging due to factors like structural/thermal distortion and layer-by-layer construction. Deviations from the intended geometry can create bottlenecks or expansions in the flow path, leading inefficient flow dynamics.
3. Internal friction is influenced by the surface roughness and texture of the tube's inner walls. Copper-based SLM-produced components often have rougher surfaces compared to those manufactured by subtractive methods, which can increase friction [31]. High internal friction results in greater energy loss, requiring post-processing, and can affect the hydraulic system's overall efficiency.

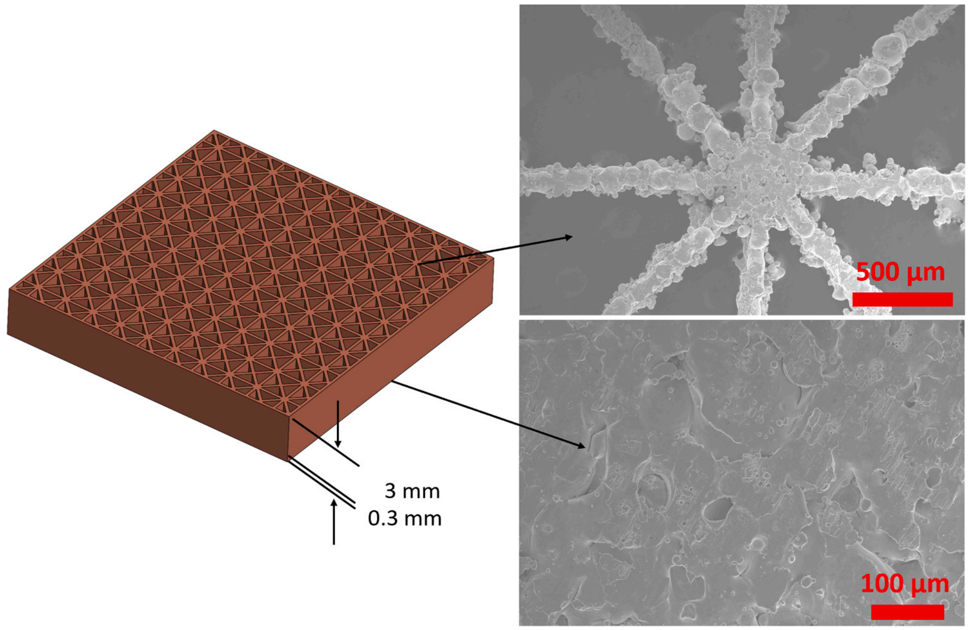

Fig. 7. Support design and SEM micrograph. Solid parts in bottom and top of the support structure are both 0.3 mm and porous support height is 3 mm.

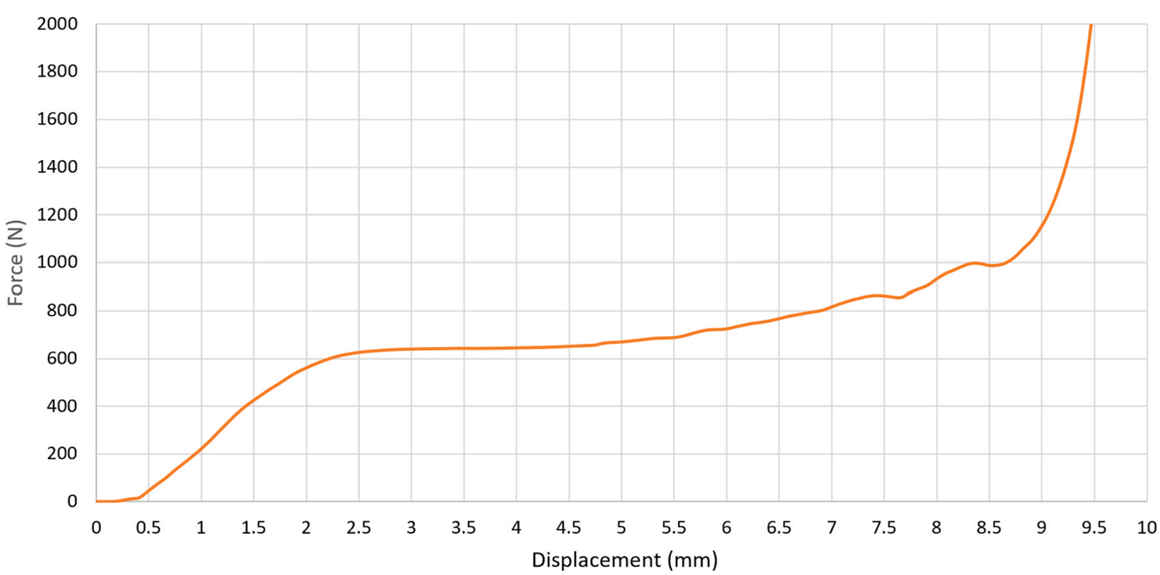

Fig. 8. Compression test results for Strut structure made from Cu–Sn alloy.

4. Unmelted particles can become dislodged and enter the flow stream, leading to blockages or erosion of the tube's internal surface. Additionally, the presence of unmelted particles can compromise the structural integrity of the tube, leading to weaknesses and potential failure points.

The experimental apparatus is shown in Fig. 10, the Tube was inserted into a PLA mold developed by 3D printing, where during printing a pause was made to insert the copper Tube, thus allowing the creation of a unique part. Then, the connections were made, two on the upper surface to carry out differential pressure measurements, and two on the side surface, to guarantee the flow inlet and outlet. The experiment consisted of creating a pressure differential to establish a flow rate of water inside the Tube. The differential pressure, ΔP, and the flow rate, Q, were measured by SM5852 Series piezoresistive differential pressure transducers and Nemesys low pressure syringe pump equipment, respectively.

The results are presented in Fig. 10, it is possible to verify that the differential pressure is directly proportional to the flow rate, which confirms with the fluid behaviour of a laminar flow described by the Hagen-Poiseuille equation defined by Eq. 2, [32].

$$Q = \frac{\pi \Delta P \quad d^4}{128 \mu L} \tag{2}$$

where Q is the flow rate (ml/hr), ΔP is the pressure differential (kPa), d is the diameter, L is the length, and μ is dynamic viscosity of the fluid, which is 1×10^{-3} Pa.s at 20 °C for distilled water. For instance, as shown in Fig. 10, at ΔP=0.33 kPa, Q=152 ml/hr, confirming the consistency between the theoretical equation and the experimental findings.

3.3. *Fin structure*

In TMDs like heat sinks, heat spreaders, or thermal interface

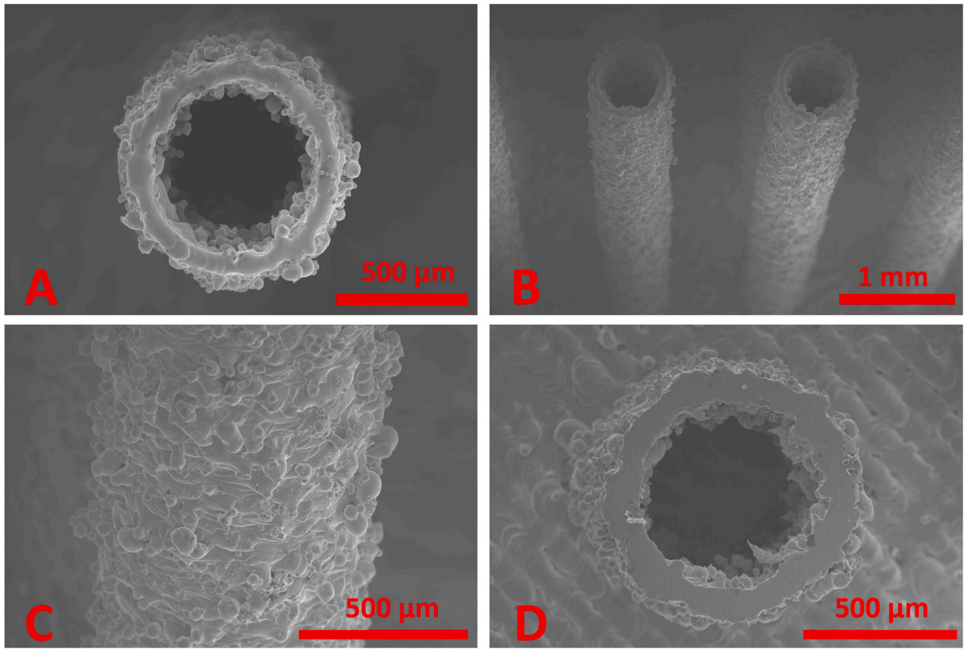

Fig. 9. SEM micrograph of as-built Tube structure, manufactured via SLM process: A and B) Top and C) lateral accuracy of hollow cylinders in different magnifications, D) Refined area of last layer for considering of densification.

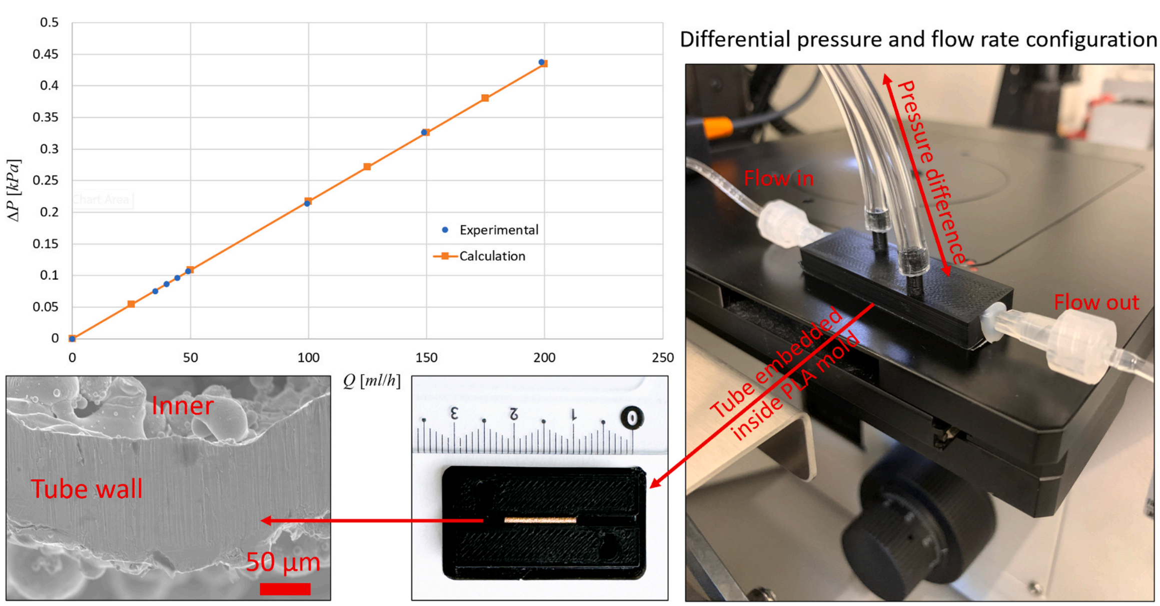

Fig. 10. Experimental apparatus and measurements of the differential pressure (ΔP) and flow rate (Q) for Tube structure (based on Eq. 1).

materials, the thin sheet cuboid structures provide a large surface area for heat dissipation. This increased surface area allows for faster cooling as heat can be more effectively radiated away. Each thin rectangular sheet (cuboid) within the Fin structure measures 0.5 × 3 × 12 mm. The SEM micrograph of the Fin structure is depicted in Fig. 11. With a defined hatch space of 0.1 mm, the laser builds the cross-section of the cuboid through 5 passes of scanning (as seen in Fig. 11C). Subsequent slight polishing of the cross-section reveals the densified, pore-free architecture (as shown in Fig. 11D).

To measure heat conduction, Fourier's law is applied to a solid sample with a diameter of 20 mm and a height of 20 mm. According to Eq. 3, the heat flux is directly proportional to the thermal gradient.

$$q = -k \quad A \quad \frac{dT}{dx} \tag{3}$$

Here, q represents the heat flux power in watts (q = IV), A is the cross-sectional area, and k is the material's thermal conductivity in watts per meter per Kelvin ($W.m^{-1}K^{-1}$). The slope of the graph (dT/dx) and consequently, the value of k will be determined using the Armfield HT11C linear device. In this test, which is illustrated in Fig. 12, the voltage and current are fixed at 9 V and 1 A, respectively, and the water flow rate through the device is set to 1.5 L/min.

Based on measurements, the value of thermal conductivity is k ~34.3 $W.m^{-1}K^{-1}$, which is much lower than the nominal thermal conductivity of pure copper (397 $W.m^{-1}K^{-1}$ [33]). The measured thermal conductivity is just ~8.6 % of that for pure Cu (showing ~91 %

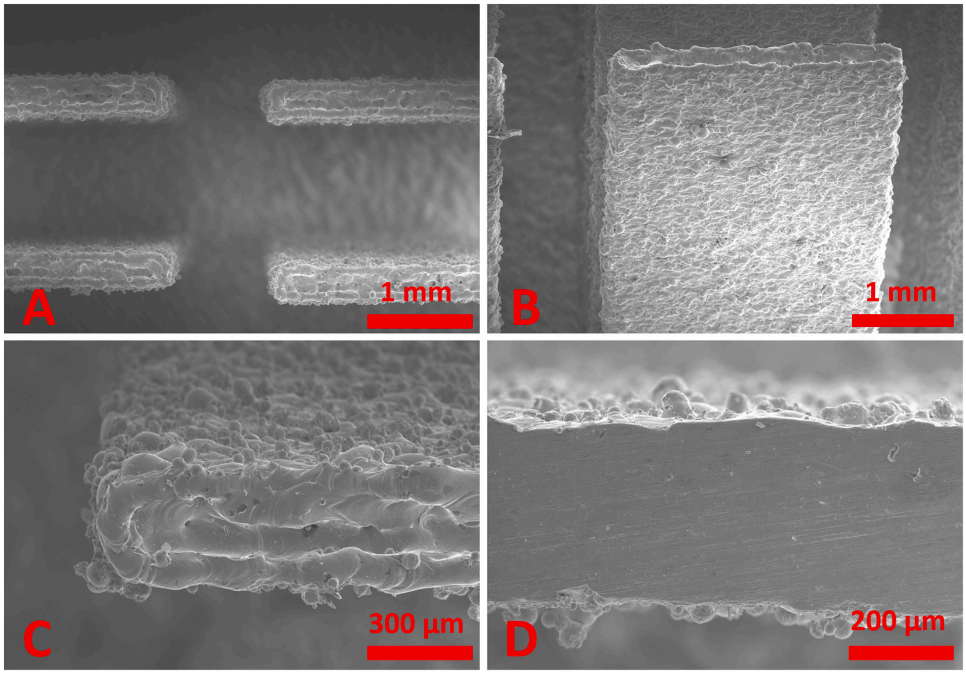

Fig. 11. SEM micrograph of as-built Fin structure manufactured through SLM process: A, B and C) Top, lateral and layers accuracy of solid areas in different magnifications, D) Refined area of last layer for considering of densification.

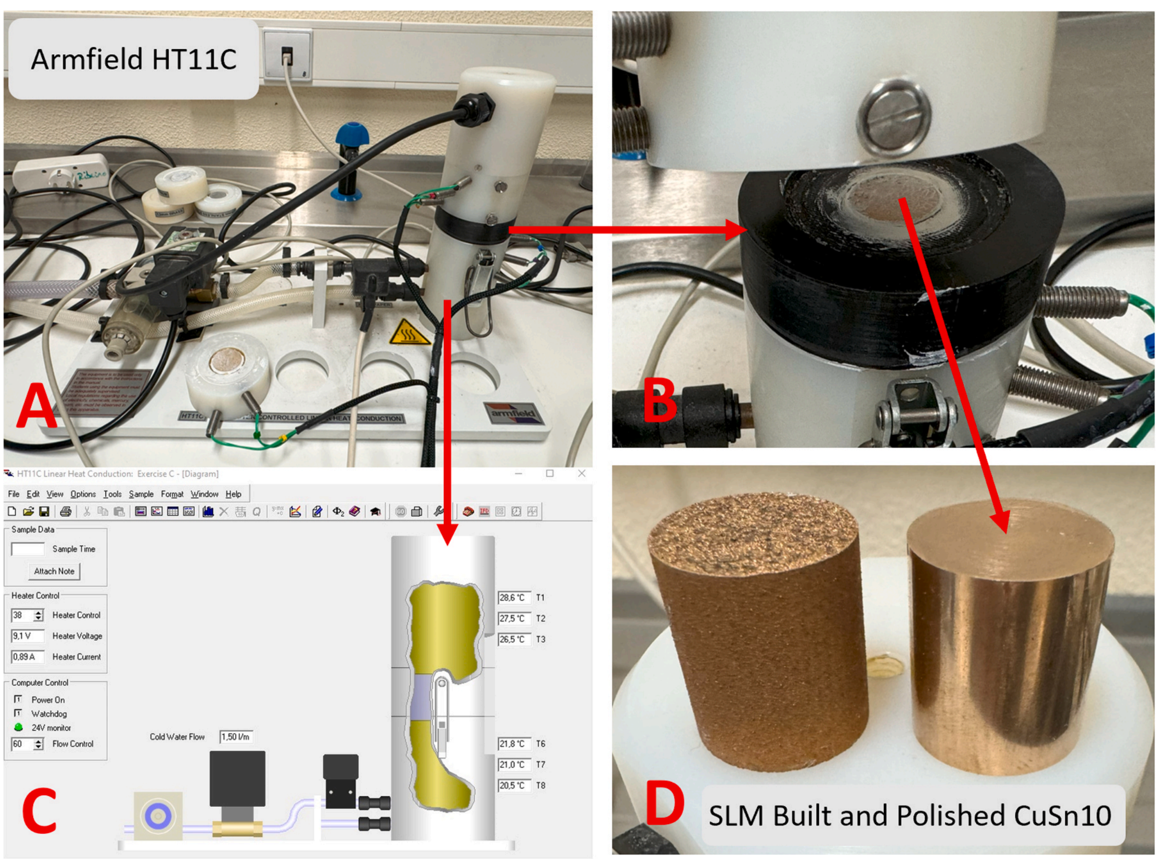

Fig. 12. Thermal conductivity test: A) Steady state linear heat conduction device, B) Ø20 × H20 mm cylindrical sample embedded inside 3D printed PLA ring and covered by thermal paste, C) Heater and higher temperature thermocouples in upper, and water-cooling system and lower temperature thermocouples in bottom of column, D) Polished sample which is applied for the test.

reduction). The reported thermal conductivity (also electrical conductivity) values for pure copper may vary slightly across different literature, possibly due to differences in test conditions, temperature, methods and the precision of the apparatus used. Despite having near-theoretical hardness and relative density, and better mechanical properties than pure copper, such results were expected based on literature [34]. The main reason for this disparity lies in the presence of 10 % tin in our material composition contributes to this variation. As demonstrated by Askeland et al. [34], the addition of just 1 wt% of tin to pure copper can reduce conductivity to 50 %. In essence, enhancing the strength of the Cu-Sn alloy comes at the expense of conductivity.

Electrical conductivity of copper is standardized at 100 % IACS (International Annealed Copper Standard) at 20°C, equivalent to ≈ $5.95 \times 10^7 S/m$. Among metals, only silver surpasses this conductivity with 105 % IACS. Since conductivity is the reciprocal of resistivity, to convert from S/m (siemens per meter) to Ω.m (ohm meter), as Eq. 4.

$$\rho = \frac{1}{\sigma} = \frac{1}{5.95 \times 10^7 \quad S/m} \approx 1.68 \times 10^{-8} \Omega.m = 1.68 \mu\Omega.cm \tag{4}$$

Where, ρ is resistivity and σ is electrical conductivity [35]. The Van der Pauw technique is employed for assessing the electrical conductivity of materials, whether solid or in thin film form. It is particularly applicable to square metals, such as our Fin structure [36] and it is shown in Fig. 13. From our experiments on a cuboid within the Fin structure (with dimensions of 1.11 cm in length, 0.292 cm in width, and 0.044 cm in thickness) made of Cu–10 % Sn alloy, we have determined the electrical conductivity and resistivity to be $\sigma = 4.72 \times 10^6 S/m$ (7.9 % of Cu) and $\rho = 2.11 \times 10^{-7} \Omega.m$, respectively.

It is worth noting that for low-alloyed copper, such as Cu–Cr–Zr, a 50 °C increase in heat treatment can improve electrical conductivity by approximately 5 % IACS [37]. This research focuses on characterizing the as-manufactured samples, avoiding any mechanical or thermal post-processing. On the other hand, the Wiedemann–Franz law establishes that the ratio of thermal conductivity (k) to electrical conductivity (σ) of metals remains constant at room temperature, denoted as L, the Lorenz number. Eq. 5 illustrates this relationship.

$$\frac{k}{\sigma} = LT, \quad (for\ Cu\text{–}10\%Sn \quad) \quad L = \frac{k}{\sigma.T} = \frac{34.3 W.m^{-1}K^{-1}}{4.72 \times 10^6 S.m^{-1} \quad \times 298 \quad K} = 2.44 \times 10^{-8} \quad V^2K^{-2} \tag{5}$$

In terms of dimensional accuracy, it is notable that 1 siemens is equivalent to 1 A per volt, while 1 watt is equal to 1 A multiplied by volt, then $V^2K^{-2} = W\Omega K^{-2}$. Monaghan et al. [38] elucidated the connection between thermal and electrical conductivity through the Lorenz constant in the context of Cu–Sn alloy, corroborating our calculations.

3.4. Mechanical and microstructural characterizations

The relative density of the fabricated samples was determined using Archimedes' immersion method for CuSn10 solid samples. The fabrication parameters included a power of 160 W, scanning speed of 320 mm/s, hatch spacing of 0.1 mm, and layer thickness of 0.025 mm. The resulting relative density was approximately 99.5 % for both Ø20 × H20 mm cylinders and 10 × 10 × 10 mm cubes, whether in their built or polished states. When compared to the results from pure copper reported in the literature, the CuSn10 (known as phosphor bronze or tin bronze) fabricated sample exhibited greater hardness and wear resistance than pure copper or equal to some other copper alloys [39–41]. The corresponding Rockwell (60 kgf), Brinell (62.5 kgf), and Vickers (50 kgf) standard test results on the sample surface were 44, 121, and 119, respectively. The details and configuration are depicted in Fig. 14.

The graph in Fig. 15 shows fluctuations in depth from about 0.2–1.8 mm across various path lengths measured for longitudinal (layer by layer assembly) and transverse direction. The parameters used to quantify surface roughness in these directions respectively are 936.49 and 939.03 nm for Ra (average roughness), 1.23 and 1.46 µm for Rq (root mean square roughness), and 5.65 and 6.17 µm for Rt (total height of the roughness profile). From the given values, it appears that the surface roughness is slightly higher in the transverse direction compared to the longitudinal direction, but in general, independent than built direction, uniform surface roughness has been achieved.

Consistent surface roughness in both longitudinal and transverse orientations (nanometre scale in depth) imply the absence of distortion caused by thermal influences during the manufacturing process, requiring an accurate scanning strategy for this printing job. In the context of this measurement, R_a represents the surface's average roughness, R_q corresponds to the square root of the cumulative squares of individual heights and depths relative to the mean line, and Rz signifies the disparity between the deepest valley and the highest peak on this Fin surface.

The majority of spherical powders utilized were generated through

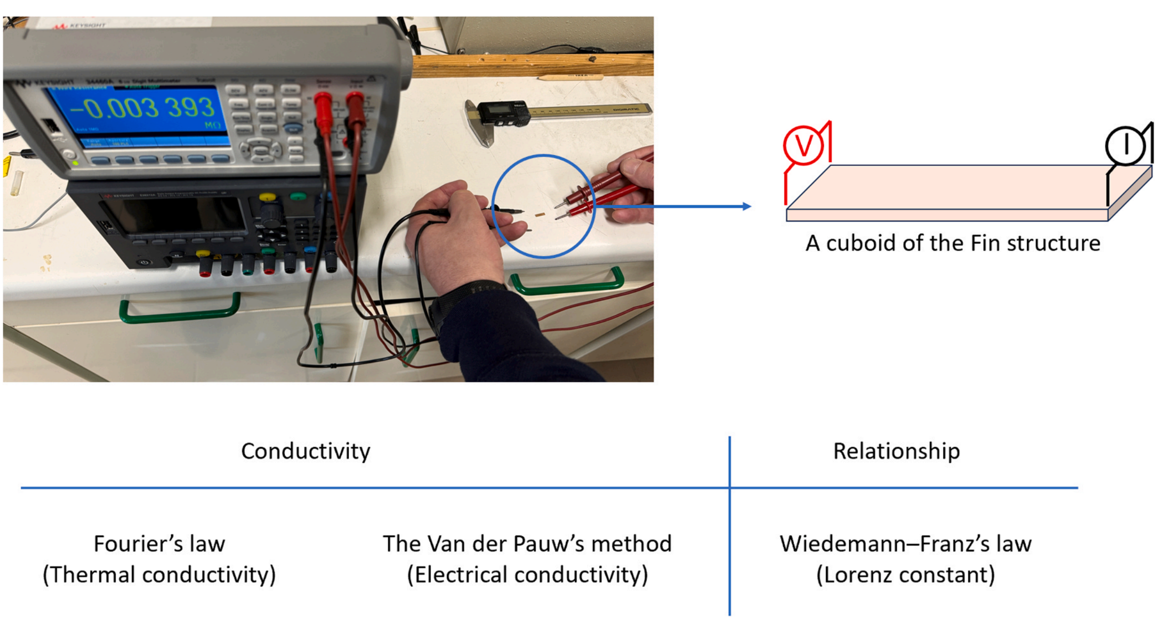

Fig. 13. Schematics of Van der Pauw configurations for electrical conductivity of thin rectangular sheet (Fin structure) and relation with thermal conductivity.

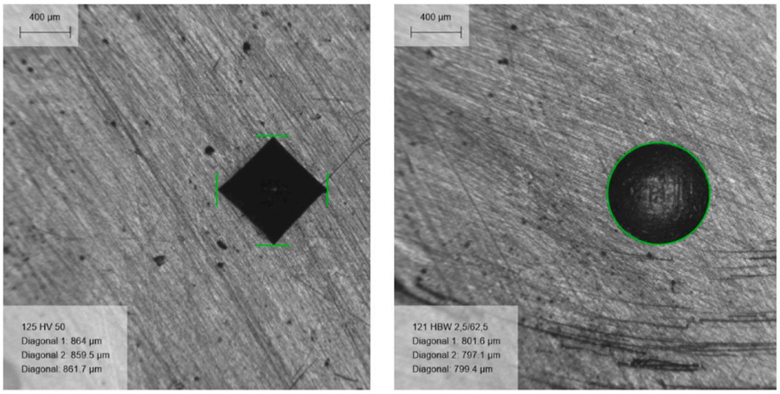

Type	Method	Hardness
Rockwell	HRA	44
Brinell	HBW 2.5/62.5	121
Vickers	HV 50	119

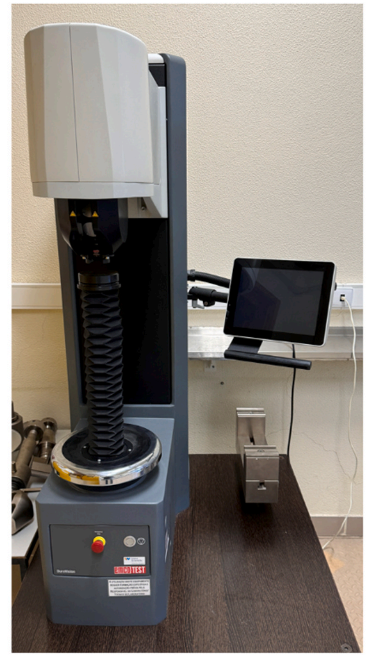

Fig. 14. Rockwell, Brinell, and Vickers test results.

gas atomization and plasma spheroidization [42]. This is crucial to achieve a finely spherical powder for metal AM processes. Such powders play a vital role in enhancing powder flowability and it results densified fabrication, contribute to reducing machine downtime, and increasing manufacturing processing speed. According to the powder producer's documentation, the CuSn10 powder exhibits a size range of 20–63 µm, a measurement that aligns with our own findings. Our assessment reveals that 10 % of the sample measures less than 19.3 µm, 50 % falls below 36.7 µm, and 90 % is smaller than 60 µm (see Fig. 2). The advantages of employing low-percent pre-alloying of Cu in L-PBF include achieving a homogeneous composition, enhanced control over microstructure, reduced sensitivity to process variations during printing, and improved mechanical properties. According to Zhao et al. [43], while microstructural features are considered comparable for both pre-alloyed and mechanically mixed powders, the latter exhibits a heterogeneous distribution of Ni and lower hardness when contrasted with samples derived from pre-alloyed Cu–Sn–Ni powder.

A thorough examination of the macro- and micro-structural features, along with mechanical analysis of copper alloys grouped by their compositions is a forthcoming objective. This systematic approach intends to include a range of well-known pre-alloyed compositions like CuSn10, CuCr1Zr, CuNi2SiCr, Cu15Ni8Sn, CuAl10, and others. Establishing a triangular relationship among i) thermo-electrical conductivity, ii) parameter optimization and printability of alloys for additive manufacturing, and iii) mechanical properties can serve as a benchmark for process standardization and proper applications.

4. Conclusion

Highly densified and hard CuSn10 alloy, suitable for various applications, is produced using the selective laser melting process. The printability and accuracy of its structural architecture are classified according to configurations such as Struts, Tubes, and Fins.

1. In the present study, SLM components were fabricated using a laser power of 160 W, a scanning speed of 320 mm/s, a hatch spacing of 0.1 mm, and a layer thickness of 0.025 mm, resulting in an energy density of 200 J/mm^3. Lower scanning speed was employed to overcome the balling phenomenon, and a reduced laser power was used to address the high thermal conductivity of copper.
2. The current study on the well-known copper alloy, CuSn10 (phosphor bronze or tin bronze), highlights that alloying pure copper significantly impacts both thermal and electrical conductivities. However, it enhances strength and low laser power printability in the SLM process, even for complex shapes, microfabrication, and thin-walled structures.
3. Having recorded values of 34.3 W.m^{-1}K^{-1} in thermal conductivity, 4.72×10^6 S/m in electrical conductivity, it exhibits ~90 % reduction over pure Cu, however, in hardness measurements, SLMed CuSn10 showed a strength of 119 HV-50, which is 110 % of Copper's strength.
4. The surface roughness in the built or transverse directions are both ~6 µm. This indicates the potential to manufacture structures that are independent of the build direction, allowing for application without the need for polishing or post-processing for thin-walled sheets.
5. A lightweight, porous lattice structure featuring struts with a diameter of 200 µm, a height of 12 mm, and a volume fraction of 33 %, can withstand a 1 kN force load and deform by 9 mm before reaching the yielding point. This makes it a potential load-bearing architecture for small-scale and compact electronic devices.
6. While the flow rate changes from 0 to 200 ml/hr, the pressure differential for micro-pipe shifts from 0 to 0.44 kPa for a Tube with an inner diameter of 500 µm, outer diameter of 1 mm, and a length greater than 10 mm. The alignment of theoretical and experimental data indicates that the internal frictional resistance caused by unmelted powder particles is negligible due to dimensional accuracy.
7. Although Cu-10 % Sn is classified as low-alloyed copper, it significantly impacts the thermo-electrical conductivity of the material. Therefore, it is recommended for use in TMD devices where strength and complex/porous shapes are prioritized.

CRediT authorship contribution statement

Sérgio I. Lopes: Data curation, Funding acquisition, Project administration. **Ramin Rahmani:** Writing – original draft, Investigation, Conceptualization. **Rúben Couto:** Formal analysis, Resources.

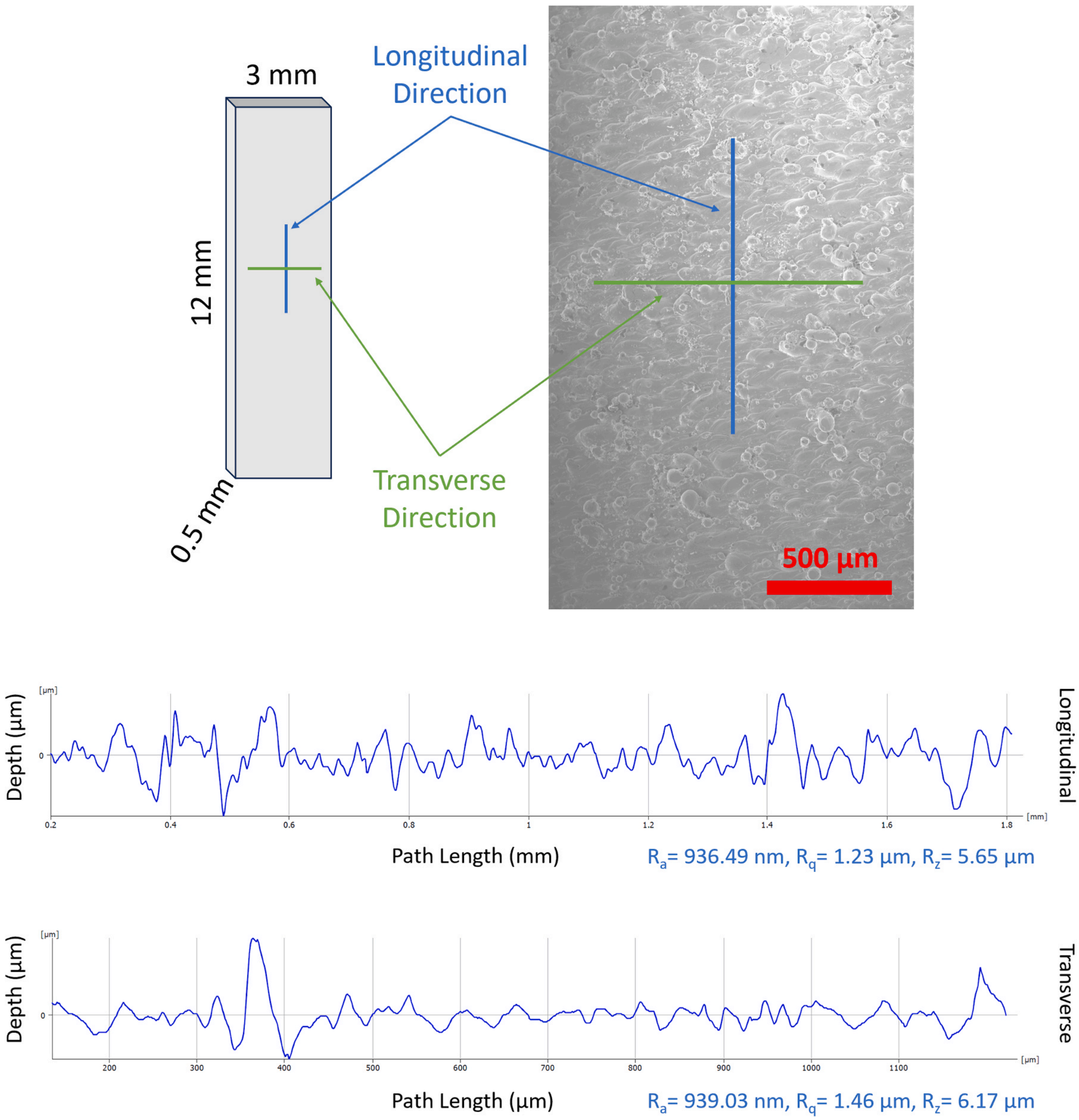

Fig. 15. Distribution of surface roughness in both directions: Top, longitudinal and Bottom, transverse directions of Fin structure and its SEM micrograph. Each block of Fin has dimension of 0.5×3×12 mm.

Joao C C Abrantes: Writing – review & editing, Validation, Supervision. **Abrar Hussain:** Resources, Investigation. **Alexandre M Afonso:** Software, Investigation. **Javad Karimi:** Writing – review & editing, Software, Methodology. **Himanshu S Maurya:** Investigation, Formal analysis. **Rahul Kumar:** Visualization, Conceptualization. **Sergio I Lopes:** Project administration, Funding acquisition, Data curation. **Ruben Couto:** Resources, Formal analysis. **João C.C. Abrantes:** Supervision, Writing – review & editing. **Pedro R Resende:** Methodology, Formal analysis, Conceptualization.

Declaration of Competing Interest

The authors declare that they have no known competing financial interests or personal relationships that could have appeared to influence the work reported in this paper.

Acknowledgements

This work received funding from Missão Interface, an operation that offers public base funding for Technology and Innovation Centers (CTI) with project code of N.º 03/C05-i02/2022 as part of the Portuguese Plano de Recuperação e Resiliência (PRR). Ramin Rahmani funded by operation NORTE-06–3559-FSE-000226, Norte Portugal Regional Operational Program (NORTE 2020), under the PORTUGAL 2020 Partnership Agreement, through the European Social Fund (ESF). This work was also developed within the scope of the proMetheus—Research Unit on Materials, Energy, and Environment for Sustainability project, FCT Ref. UID/05975/2020, financed by national funds through the FCT/MCTES. In addition, the authors thank T. Rodrigues from CEFT for help with pressure measurements. Javad Karimi would like to acknowledge the AiF- Arbeitsgemeinschaft industrieller Forschungsvereinigungen (IKAF, 01.3351).

Annex

For a quick overview, two tables summarizing the article's outcomes are provided here. The abbreviated results from this article are presented in Table 1. Also, the main benefits and drawbacks of each structure are illustrated in Table 2.

Table 1
Brief findings from this article.

Structure	Property	Value	Units
General	XRD pattern	α-Cu and δ-Cu40.5Sn11	Phases
General	Powder density	≥ 4.7	g/cm^3
Strut	Compression strength	1	kN
Strut	Hardness	119	HV−50
Tube	Pressure and flow rate	ΔP=0.44 kPa ~ Q=200	kPa, ml/hr
Tube	Diameter precision	inner 0.5, outer 1	mm
Fin	Electrical conductivity	4.72×10^6	S/m
Fin	Surface roughness	~ 6	µm
General	Energy density	200	J/mm^3
General	Thermal conductivity	34.3	$W\ m^{-1}\ K^{-1}$

Table 2
Benefits and drawbacks of structures discussed in this article.

Structure	**Benefit**	**Drawback**
General	Higher hardness and strength than pure copper	Thermal and electrical conductivity are lower than pure copper
Strut	Lightness and complex architecture for electronic devices	Sticked particles to lattice struts and difficulty of cleaning
Tube	High control on pneumatic and hydraulic systems	Distortion possibility for micro-pipes during post-processing
Fin	Fabrication of micro-sheets with fine surface	Difficulty in electrical measurements due to small size

References

[1] T.G. Spears, S.A. Gold, In-process sensing in selective laser melting (SLM) additive manufacturing, Integr. Mater. Manuf. Innov. 5 (2016) 16–40, https://doi.org/10.1186/s40192-016-0045-4.
[2] R. Rahmani, M. Brojan, M. Antonov, K.G. Prashanth, Perspectives of metal-diamond composites additive manufacturing using SLM-SPS and other techniques for increased wear-impact resistance, Int. J. Refract. Met. Hard Mater. 88 (2020) 105192, https://doi.org/10.1016/j.ijrmhm.2020.105192.
[3] T.-T. Ikeshoji, K. Nakamura, M. Yonehara, Ken Imai, Hideki Kyogoku, Selective laser melting of pure copper, JOM 70 (2018) 396–400, https://doi.org/10.1007/s11837-017-2695-x.
[4] J. Tian, W. Zhu, Q. Wei, S. Wen, S. Li, B. Song, Y. Shi, Process optimization, microstructures and mechanical properties of a Cu-based shape memory alloy fabricated by selective laser melting, J. Alloy. Compd. 785 (2019) 754–764, https://doi.org/10.1016/j.jallcom.2019.01.153.
[5] B. Luo, D. Li, C. Zhao, Z. Wang, Z. Luo, W. Zhang, A low Sn content Cu-Ni-Sn alloy with high strength and good ductility, Mater. Sci. Eng.: A 746 (2019) 154–161, https://doi.org/10.1016/j.msea.2018.12.120.
[6] X. Yan, C. Chang, D. Dong, S. Gao, W. Ma, M. Liu, H. Liao, S. Yin, Microstructure and mechanical properties of pure copper manufactured by selective laser melting, Mater. Sci. Eng.: A 789 (2020) 139615, https://doi.org/10.1016/j.msea.2020.139615.
[7] Z. Ma, D.Z. Zhang, F. Liu, J. Jiang, M. Zhao, T. Zhang, Lattice structures of Cu-Cr-Zr copper alloy by selective laser melting: microstructures, mechanical properties and energy absorption, Mater. Des. 187 (2020) 108406, https://doi.org/10.1016/j.matdes.2019.108406.
[8] R. Rahmani, J. Karimi, P.R. Resende, J.C.C. Abrantes, S.I. Lopes, Overview of selective laser melting for industry 5.0: toward customizable, sustainable, and human-centric technologies, Machines 11 (2023) 522, https://doi.org/10.3390/machines11050522.
[9] R. Rahmani, K.G. Prashanth, S.I. Lopes, Selective Laser Melting and Spark Plasma Sintering: A Perspective on Functional Biomaterials, J. Funct. Biomater. 14 (2023) 521, https://doi.org/10.3390/jfb14100521.
[10] S.-G. Kang, R. Gainov, D. Heußen, S. Bieler, Z. Sun, K. Weinberg, G. Dehm, R. Ramachandramoorthy, Green laser powder bed fusion based fabrication and rate-dependent mechanical properties of copper lattices, Mater. Des. 231 (2023) 112023, https://doi.org/10.1016/j.matdes.2023.112023.
[11] X. Lingqin, C. Guang, Z. Luyu, L. Pan, Explore the feasibility of fabricating pure copper parts with low-laser energy by selective laser melting, Mater. Res. Express 7 (2020) 106509, https://doi.org/10.1088/2053-1591/abbd08.
[12] L. Kaden, G. Matthäus, T. Ullsperger, H. Engelhardt, M. Rettenmayr, A. Tünnermann, S. Nolte, Selective laser melting of copper using ultrashort laser pulses, Appl. Phys. A 123 (2017) 596, https://doi.org/10.1007/s00339-017-1189-6.
[13] J. Wang, X.L. Zhou, J. Li, M. Brochu, Y.F. Zhao, Microstructures and properties of SLM-manufactured Cu-15Ni-8Sn alloy, Addit. Manuf. 31 (2020) 100921, https://doi.org/10.1016/j.addma.2019.100921.
[14] Z. Ma, K. Zhang, Zh Ren, D.Z. Zhang, G. Tao, H. Xu, Selective laser melting of Cu–Cr–Zr copper alloy: Parameter optimization, microstructure and mechanical properties, J. Alloy. Compd. 828 (2020) 154350, https://doi.org/10.1016/j.jallcom.2020.154350.
[15] R. Rahmani, M. Antonov, L. Kollo, Y. Holovenko, K.G. Prashanth, Mechanical behavior of Ti6Al4V Scaffolds Filled with CaSiO3 for implant applications, Appl. Sci. 9 (2019) 3844, https://doi.org/10.3390/app9183844.
[16] R. Rahmani, M. Rosenberg, A. Ivask, L. Kollo, Comparison of mechanical and antibacterial properties of TiO2/Ag ceramics and Ti6Al4V-TiO2/Ag composite materials using combining SLM-SPS techniques, Metals 9 (2019) 874, https://doi.org/10.3390/met9080874.
[17] S.H.W. Lee, H.L. Choo, S.H. Mok, X.Y. Cheng, Y.H.P. Manurung, Fabrication of porous metallic materials by controlling the processing parameters in selective laser melting process, AIP Conf. Proc. 2233 (2020) 020016. 〈https://doi.org/10.1063/5.0001632〉.
[18] M. Król, P. Snopiński, J. Hajnyš, M. Pagáč, D. Łukowiec, Selective laser melting of 18NI-300 maraging steel, Materials 13 (2020) 4268, https://doi.org/10.3390/ma13194268.
[19] B. Xie, Y. Fan, S. Zhao, Characterization of Ti6Al4V powders produced by different methods for selective laser melting, Mater. Res. Express 8 (2021) 076510, https://doi.org/10.1088/2053-1591/ac10d1.
[20] F. Chu, K. Zhang, H. Shen, M. Liu, W. Huang, X. Zhang, E. Liang, Z. Zhou, L. Lei, J. Hou, A. Huang, Influence of satellite and agglomeration of powder on the processability of AlSi10Mg powder in Laser Powder Bed Fusion, J. Mater. Res. Technol. 11 (2021) 2059–2073, https://doi.org/10.1016/j.jmrt.2021.02.015.
[21] K. Molan, R. Rahmani, D. Krklec, M. Brojan, D. Stopar, Phi 6 Bacteriophage Inactivation by Metal Salts, Metal Powders, and Metal Surfaces, Viruses 14 (2022) 204, https://doi.org/10.3390/v14020204.
[22] R. Rahmani, K. Molan, M. Brojan, K.G. Prashanth, D. Stopar, High virucidal potential of novel ceramic–metal composites fabricated via hybrid selective laser melting and spark plasma sintering routes, Int. J. Adv. Manuf. Technol. (2022) 1–14, https://doi.org/10.1007/s00170-022-08878-x.
[23] C. Deng, J. Kang, T. Feng, Y. Feng, X. Wang, P. Wu, Study on the selective laser melting of CuSn10 powder, Materials 11 (2018) 614, https://doi.org/10.3390/ma11040614.
[24] R. Rahmani, J. Karimi, N. Kamboj, R. Kumar, M. Brojan, A. Tchórz, G. Skrabalak, S. I. Lopes, Fabrication of localized diamond-filled copper structures via selective laser melting and spark plasma sintering, Diam. Relat. Mater. 136 (2023) 109916, https://doi.org/10.1016/j.diamond.2023.109916.
[25] Y. Zhou, Y. Fang, J. Wang, L. Xu, D. Wang, Process parameter optimization on selective laser melting of CuSn10 powders based on response surface methodology, J. Phys.: Conf. Ser. 2262 (2022) 012002, https://doi.org/10.1088/1742-6596/2262/1/012002.

[26] Z. Li, G. Zhao, H. Wang, G. Gao, S. Chen, D. Yang, Y. Fan, G. Zhang, H. Xu, Microstructure and tribological behaviors of diffusion bonded powder sintered Cu–Sn based alloys, Mater. Res. Express 8 (2021) 116505, https://doi.org/10.1088/2053-1591/ac31ff.

[27] C. Zeng, B. Zhang, A. Hemmasian Ettefagh, H. Wen, H. Yao, W.J. Meng, S. Guo, Mechanical, thermal, and corrosion properties of Cu-10Sn alloy prepared by laser-powder-bed-fusion additive manufacturing, Addit. Manuf. 35 (2020) 101411, https://doi.org/10.1016/j.addma.2020.101411.

[28] R. Rahmani, N. Kamboj, M. Brojan, M. Antonov, K.G. Prashanth, Hybrid metal-ceramic biomaterials fabricated through powder bed fusion and powder metallurgy for improved impact resistance of craniofacial implants, Journal of, Materialia 24 (2022) 101465, https://doi.org/10.1016/j.mtla.2022.101465.

[29] R. Rahmani, M. Brojan, M. Antonov, Lightweight 3D printed Ti6Al4V-AlSi10Mg hybrid composite for impact resistance and armor piercing shielding, J. Mater. Res. Technol. 9 (2020) 13842–13854, https://doi.org/10.1016/j.jmrt.2020.09.108.

[30] Y.H. Choong, M. Krishnan, M. Gupta, Recent advances in the 3D printing of pure copper functional structures for thermal management devices, Technologies 11 (2023) 141, https://doi.org/10.3390/technologies11050141.

[31] J. Pakkanen, F. Calignano, F. Trevisan, M. Lorusso, E.P. Ambrosio, D. Manfredi, P. Fino, Study of internal channel surface roughnesses manufactured by selective laser melting in aluminum and titanium alloys, Met. Mater. Trans. A 47 (2016) 3837–3844, https://doi.org/10.1007/s11661-016-3478-7.

[32] J.W. Gooch, Hagen-Poiseuille Equation. Encyclopedic Dictionary of Polymers, Springer, New York, NY, 2011, https://doi.org/10.1007/978-1-4419-6247-8_5752.

[33] D.R.H. Jones, M.F. Ashby, Chapter 32-thermal conductivity and specific heat, Eng. Mater. 1, Fifth Ed. (2019) 515–530, https://doi.org/10.1016/B978-0-08-102051-7.00032-4.

[34] D.R. Askeland, P.P. Phulé, The science and engineering of materials, Springer Book Publication, 4th Edition (2003). ISBN 978-0-495-29602-7.

[35] W. Lowrie, A. Fichtner, Fundamentals of Geophysics, Cambridge University Press, 2007. ISBN 978-05-2185-902-8.

[36] G. Rietveld, C.V. Koijmans, L.C.A. Henderson, M.J. Hall, S. Harmon, P. Warnecke, B. Schumacher, DC conductivity measurements in the Van der Pauw geometry, IEEE Trans. Instrum. Meas. 52 (2003) 449–453, https://doi.org/10.1109/TIM.2003.809917.

[37] P. Guan, X. Chen, P. Liu, F. Sun, C. Zhu, H. Zhou, S. Fu, Z. Wu, Y. Zhu, Effect of selective laser melting process parameters and aging heat treatment on properties of CuCrZr alloy, Mater. Res. Express 6 (2019) 1165c1, https://doi.org/10.1088/2053-1591/ab4e2f.

[38] B.J. Monaghan, J.G.J. Neale, L. Chapman, Some thermal properties of a copper–tin alloy, Int. J. Thermophys. 20 (1999) 1051–1060, https://doi.org/10.1023/A:1022694518254.

[39] Z. Mao, D.Z. Zhang, P. Wei, K. Zhang, Manufacturing feasibility and forming properties of Cu-4Sn in selective laser melting, Materials 10 (2017) 333, https://doi.org/10.3390/ma10040333.

[40] F. Sun, P. Liu, X. Chen, H. Zhou, P. Guan, B. Zhu, Mechanical properties of high-strength Cu–Cr–Zr alloy fabricated by selective laser melting, Materials 13 (2020) 5028, https://doi.org/10.3390/ma13215028.

[41] R. Rahmani, M. Antonov, K.G. Prashanth, The impact resistance of highly densified metal alloys manufactured from gas-atomized prealloyed powders, Coatings 11 (2021) 216, https://doi.org/10.3390/coatings11020216.

[42] W.S.W. Harun, M.S.I.N. Kamariah, N. Muhamad, S.A.C. Ghani, F. Ahmad, Z. Mohamed, A review of powder additive manufacturing processes for metallic biomaterials, Powder Technol. 327 (2018) 128–151, https://doi.org/10.1016/j.powtec.2017.12.058.

[43] C. Zhao, Z. Wang, D. Li, M. Xie, L. Kollo, Z. Luo, W. Zhang, K.G. Prashanth, Comparison of additively manufacturing samples fabricated from pre-alloyed and mechanically mixed powders, J. Alloy. Compd. 830 (2020) 154603, https://doi.org/10.1016/j.jallcom.2020.154603.